

Tunable Modal Birefringence in a Low-Loss Van Der Waals Waveguide

Debo Hu, Ke Chen, Xinzhong Chen, Xiangdong Guo, Mengkun Liu,* and Qing Dai*

van der Waals (vdW) crystals are promising candidates for integrated phase retardation applications due to their large optical birefringence. Among the two major types of vdW materials, the hyperbolic vdW crystals are inherently inadequate for optical retardation applications since the supported polaritonic modes are exclusively transverse-magnetic (TM) polarized and relatively lossy. Elliptic vdW crystals, on the other hand, represent a superior choice. For example, molybdenum disulfide (MoS_2) is a natural uniaxial vdW crystal with extreme elliptic anisotropy in the frequency range of optical communication. Both transverse-electric (TE) polarized ordinary and TM polarized extraordinary waveguide modes can be supported in MoS_2 microcrystals with suitable thicknesses. In this work, low-loss transmission of these guided modes is demonstrated with nano-optical imaging at the near-infrared (NIR) wavelength (1530 nm). More importantly, by combining theoretical calculations and NIR nanoimaging, the modal birefringence between the orthogonally polarized TE and TM modes is shown to be tunable in both sign and magnitude via varying the thickness of the MoS_2 microcrystal. This tunability represents a unique new opportunity to control the polarization behavior of photons with vdW materials.

Phase retardation elements such as waveplates and compensators are important polarization management components that play an essential part in modern optical communication systems.^[1,2] Anisotropic crystals exhibiting optical birefringence are the fundamental building blocks of these bulk components.^[3,4] With the advancement of nano-optics in the quantum era, miniaturization and integration of these phase retardation components become imperative.^[5–7] In analogy with their bulk counterparts which introduce path difference between orthogonally polarized light through optical birefringence, the integrated optical phase retardation elements import

path difference between orthogonally polarized guided modes via the modal birefringence of the waveguides.^[8] Unlike the bulk birefringence which is predefined by the material, the modal birefringence of waveguides are tunable with constituent materials and waveguide geometry.^[9] However in practice the manufacture of integrated phase retarders with designed modal birefringence is particularly challenging because of their stringent fabrication tolerance.^[10] Therefore, new materials allowing layer-by-layer control and fine mechanical processing are highly demanded.

Due to the difference between their interlayer and intralayer bonding strengths, van der Waals (vdW) crystals are both mechanically and optically anisotropic.^[11,12] In light of this intrinsic out-of-plane bi-anisotropy, vdW crystals are promising materials for the phase retardation applications in integrated optical circuits: the mechanical anisotropy per-

mits the precise layer-by-layer manufacturing of the waveguide structure while the optical anisotropy provides one more degree of freedom to control its modal birefringence. vdW crystals with hyperbolic optical responses such as hexagonal boron nitride ($h\text{-BN}$)^[13,14] and α -phase molybdenum trioxide ($\alpha\text{-MoO}_3$)^[15,16] have been demonstrated to support highly confined phonon polaritons in the mid-infrared (MIR) frequency range. However, these polaritonic modes are inherently inadequate for the integrated phase retardation applications (polariton-assisted polarization control of far-field light with metasurfaces made of vdW materials is possible^[17]), as a result of their inevitable transmission loss (imposed by the Kramers–Kronig relationships between dispersion and dissipation^[18,19]) and the absence of transverse-electric (TE) polarized modes.^[20,21] An alternative way is to resort to vdW crystals with elliptic anisotropy at frequencies far away from any resonant absorption bands. In such case, the imaginary parts of the permittivity tensor are usually negligible and result in positive real parts.^[22] The near-zero imaginary parts of permittivity guarantee the low-loss transmission of the supported waveguide modes, while the positive real parts allow the co-occurrence of TE and transverse-magnetic (TM) polarized modes. Transition metal dichalcogenides (TMDs) are expected to exhibit elliptic light dispersion in a broad frequency range (note that $h\text{-BN}$ is also elliptically anisotropic out of its Reststrahlen bands, the reason TMDs are better for our proposed applications will be discussed at a later stage);^[23]

Dr. D. B. Hu, K. Chen, X. D. Guo, Prof. Q. Dai
Division of Nanophotonics
CAS Center for Excellence in Nanoscience
National Center for Nanoscience and Technology
Beijing 100190, China
E-mail: daiq@nanoctr.cn

X. Z. Chen, Prof. M. K. Liu
Department of Physics
Stony Brook University
Stony Brook, NY 11794, USA
E-mail: mengkun.liu@stonybrook.edu

 The ORCID identification number(s) for the author(s) of this article can be found under <https://doi.org/10.1002/adma.201807788>.

DOI: 10.1002/adma.201807788

this elliptic anisotropy together with the single-layer precisely modifiable structure^[24,25] of TMDs would permit fine-tuning of the modal birefringence between TE and TM polarized modes, and thus enable the implementation of phase retarders in integrated optical circuits.

In this work, we choose molybdenum disulfide (MoS₂)^[26–29] as a representative for TMDs to introduce the concept of vdW optical phase retarders. We first show the low-loss transmission of waveguide modes in MoS₂ in the near-infrared (NIR) frequency range by comparing the near-field imaging results between MoS₂ and *h*-BN at the same excitation wavelength $\lambda = 1530$ nm. We then demonstrate that the modal birefringence between the orthogonally polarized ordinary (TE) and extraordinary (TM) guided modes can be fine-tuned by varying the thickness of the MoS₂ crystal, as a result of its extreme out-of-plane elliptic anisotropy (the optical birefringence of MoS₂ at 1530 nm is about 1.4,^[30] much larger than those of common non-vdW crystals and the state-of-the-art barium titanium sulfide^[31,32]). Functionalities of the proposed vdW zero-order half-wave plates and phase-matched waveguide will also be discussed via numerical simulations.

Near-field optical images of the waveguide modes in MoS₂ and *h*-BN were obtained by scattering-type scanning near-field optical microscopy (s-SNOM).^[33–37] (see the Experimental Section). **Figure 1a** is the schematic diagram of the experimental setup for MoS₂ NIR nanoimaging. The MoS₂ microcrystal is exfoliated onto standard silicon wafer with a 300 nm thick SiO₂ top layer. The laser beam with a wavelength of 1530 nm is focused onto the apex of the s-SNOM tip to excite both ordinary and extraordinary guided modes in the air–MoS₂–SiO₂ three-layer waveguide. These modes spread circularly in the waveguide until they come across the sharp edge of the MoS₂ microcrystal. At the edge, part of these guided modes get scattered into the far field and interfere with the tip-scattered light at the photodetector (inset of Figure 1a). With the sample raster-scanning under the s-SNOM tip, an interference pattern can therefore be recorded. Since their paths back to the photodetector are both oblique to the MoS₂ surface, the optical path difference between the tip-scattered and the edge-scattered light depends on the direction of the MoS₂ edge, and therefore the s-SNOM images of the guided modes are strongly edge-orientation dependent. To reduce the complexity in data analysis, we align the edge of MoS₂ vertically along the direction of the AFM cantilever and scan horizontally. In this way, the obtained apparent effective indices of refraction for the guided modes differentiate from the genuine ones only by a constant geometrical factor $\cos \alpha \sin \beta$ (α is the angle between the illumination wavevector k_0 and its projection in the x – y plane k_{xy} , β is the angle between k_{xy} and the investigated sample edge).^[30,38] To compare the transmission losses of the guided modes in MoS₂ and *h*-BN, we repeated the same experiment on *h*-BN using the same setup.

Experimental results for the near-field imaging of a 110 nm thick MoS₂ and a 270 nm thick *h*-BN microcrystals are compared side by side in Figure 1b,c. It is obvious to see that the waveguide mode in MoS₂ exhibits a relatively higher wavelength compression and a much longer propagation distance than that in *h*-BN. To quantify the transmission losses of the guided modes, we fit the experimental data with a damped cosine wave

$$s(x) = A \cos(q_1 x + B) \frac{\exp(-q_2 x)}{x^\eta} + C \quad (1)$$

In Equation (1), $s(x)$ is the magnitude of the near-field signal, A is the amplitude of cosine wave, B is a phase constant, C is the DC component of near-field signal, q_1 is the apparent wavevector of waveguide modes, q_2 is the damping factor, and η is a factor accounting for the circular spreading of tip-launched waveguide modes. The fitted curves are overlaid to the near-field fringes in Figure 1b,c. The inverse damping ratio $\gamma_p^{-1} = q_1/q_2$ is 90.9 for MoS₂ and 45.6 for *h*-BN. This disparity in transmission loss is counter-intuitive at the first glance since both MoS₂ and *h*-BN are dielectric media at the wavelength of 1530 nm and thus only minor scattering loss from the fabrication imperfection is expected. However, the experimental results can be understood if we take the finite layer thickness (300 nm) of SiO₂ into consideration and regard both the MoS₂ and the *h*-BN heterostructures as leaky mode waveguides,^[39] in which all the guided modes with effective indices of refraction less than the refractive index of Si (3.5) tend to tunnel through the SiO₂ layer and dissipate in the Si layer below. The guided modes are better confined in MoS₂ in both vertical and horizontal directions as a result of its relatively higher refractive indices than those of *h*-BN,^[30] as demonstrated by numerical simulations in Figure 1d,e. This better vertical confinement makes the guided modes in MoS₂ less likely to leak out and therefore exhibit lower loss in practice.

Of course, the low transmission loss alone does not necessarily make TMDs of unique appeal in integrated optical phase retardation applications; it is the extreme elliptic anisotropy in the technologically important NIR frequency range that holds the key. In isotropic materials, different guided modes are forbidden from possessing the same effective index of refraction by the optical nondegeneracy theorem (see Section S1 in the Supporting Information for details). Therefore, phase matching between different guided modes in this kind of waveguide can never be achieved and the modal birefringence is only tunable in magnitude in a limited range.^[40] On the contrary, the nondegeneracy between orthogonally polarized guided modes can be violated in a planar waveguide comprising elliptically anisotropic media (see Section S2 in the Supporting Information for details) and the modal birefringence is tunable in both sign and magnitude in a wide range. In the following, to theoretically investigate the modal birefringence tunability of vdW waveguides, we take MoS₂ and *h*-BN as representative examples again.

The characteristic equations for the TE and TM polarized guided modes in a planar waveguide made of uniaxially anisotropic guiding layer and isotropic cladding layers can be written as^[30]

$$k_0 \sqrt{n_o^2 - n_{\text{eff,TE}}^2} d = \tan^{-1} \left(\frac{\sqrt{n_{\text{eff,TE}}^2 - n_1^2}}{\sqrt{n_o^2 - n_{\text{eff,TE}}^2}} \right) + \tan^{-1} \left(\frac{\sqrt{n_{\text{eff,TE}}^2 - n_2^2}}{\sqrt{n_o^2 - n_{\text{eff,TE}}^2}} \right) + p\pi \quad (2)$$

and

$$k_0 \frac{n_o}{n_e} \sqrt{n_e^2 - n_{\text{eff,TM}}^2} d = \tan^{-1} \left(\frac{n_o n_e \sqrt{n_{\text{eff,TM}}^2 - n_1^2}}{n_1^2 \sqrt{n_e^2 - n_{\text{eff,TM}}^2}} \right) + \tan^{-1} \left(\frac{n_o n_e \sqrt{n_{\text{eff,TM}}^2 - n_2^2}}{n_2^2 \sqrt{n_e^2 - n_{\text{eff,TM}}^2}} \right) + q\pi \quad (3)$$

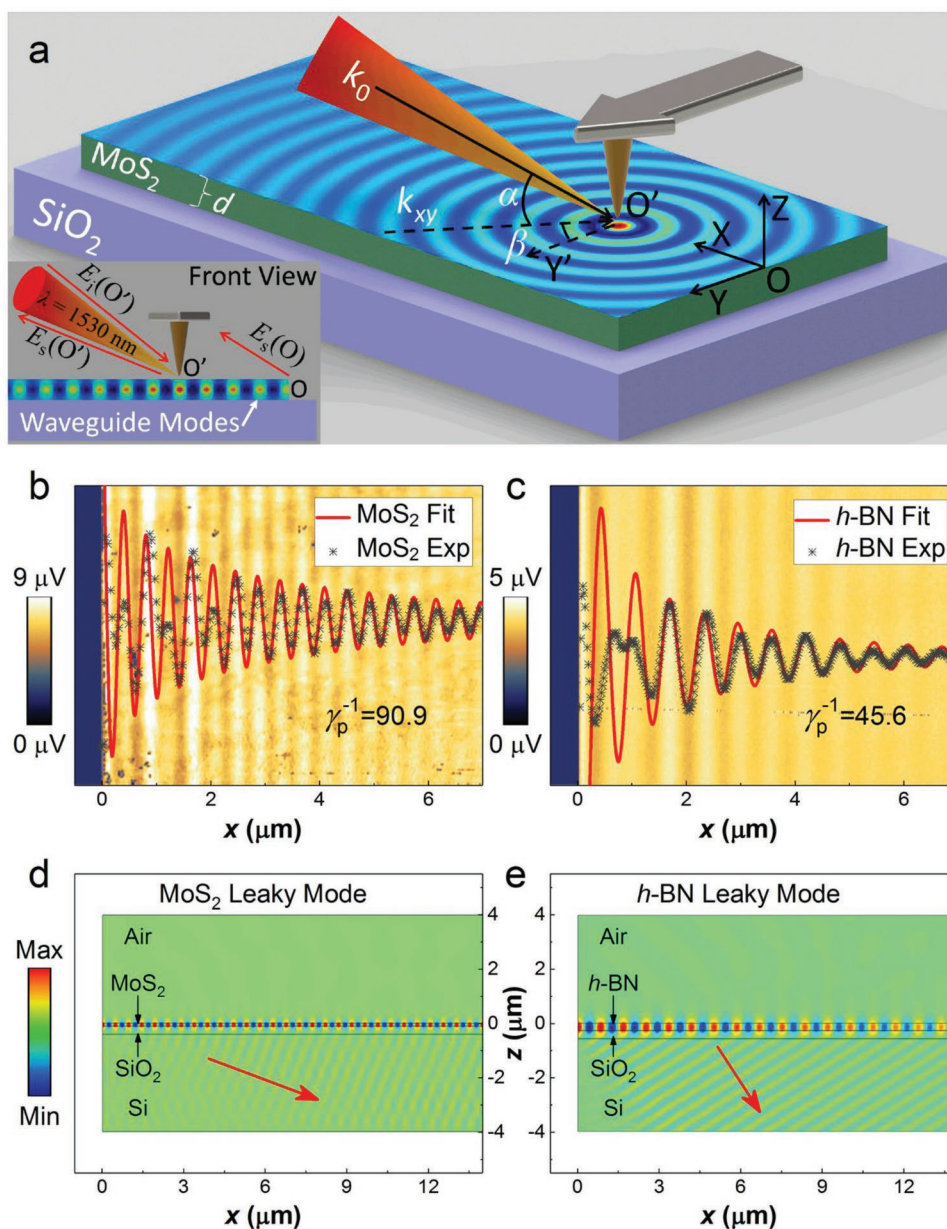


Figure 1. Optical nanoimaging of the waveguide modes in MoS₂ and *h*-BN. a) Experimental setup for MoS₂ NIR nanoimaging. The sharp edges of MoS₂ microcrystals are aligned to the γ -axis and the s-SNOM tip scans along the x -axis. α is the angle between the illumination wavevector k_0 and its projection in the x - y plane k_{xy} , β is the angle between k_{xy} and the investigated sample edge. Inset is the front view of the experimental setup, the tip-launched guided modes are scattered into free space at the sample edge and interfere with the tip-scattered light at the photodetector. b,c) NIR nanoimaging results for a 110 nm thick MoS₂ and a 270 nm thick *h*-BN microcrystals at the same excitation wavelength $\lambda = 1530$ nm, respectively. The inverse damping ratios γ_p^{-1} of the guided modes can be obtained by fitting the fringe profiles with damped cosine waves. Note that the first three experimentally obtained fringes have been left out in the fitting procedure, in both (b) and (c), to eliminate the interference from the edge-launched guided modes. d,e) Numerical simulations of the mode propagation in MoS₂ and *h*-BN, respectively. Due to the finite thickness of the SiO₂ layer, the guided modes can leak out of the waveguides and lead to the observed transmission losses in (b) and (c). Moreover, due to the lower field confinement, the guided modes in *h*-BN tunnel through the SiO₂ layer are much easier than those in MoS₂, thus suffering higher transmission loss. The red arrows indicate the propagation directions of the leaked light in Si. Note that for *h*-BN the mode leakage rate is higher than that for MoS₂.

respectively. In Equations (2) and (3), k_0 is the free-space wave-number; d is the guiding layer thickness; n_o and n_e are the ordinary and extraordinary refractive indices of the guiding layer, respectively; n_1 and n_2 are the refractive indices of superstrate and substrate layers, respectively; p and q are the order numbers of TE and TM modes, respectively; $n_{\text{eff,TE}}$ and $n_{\text{eff,TM}}$ are effective

indices of refraction for TE and TM modes, respectively. Specifically, Equations (2) and (3) can be reduced to the characteristic equations for guided modes in a planar waveguide made of exclusively isotropic materials by equalizing n_o and n_e .^[41]

Shown in Figure 2a are the thickness dispersions of the four lowest-order guided modes in the air–MoS₂–SiO₂ three-layer

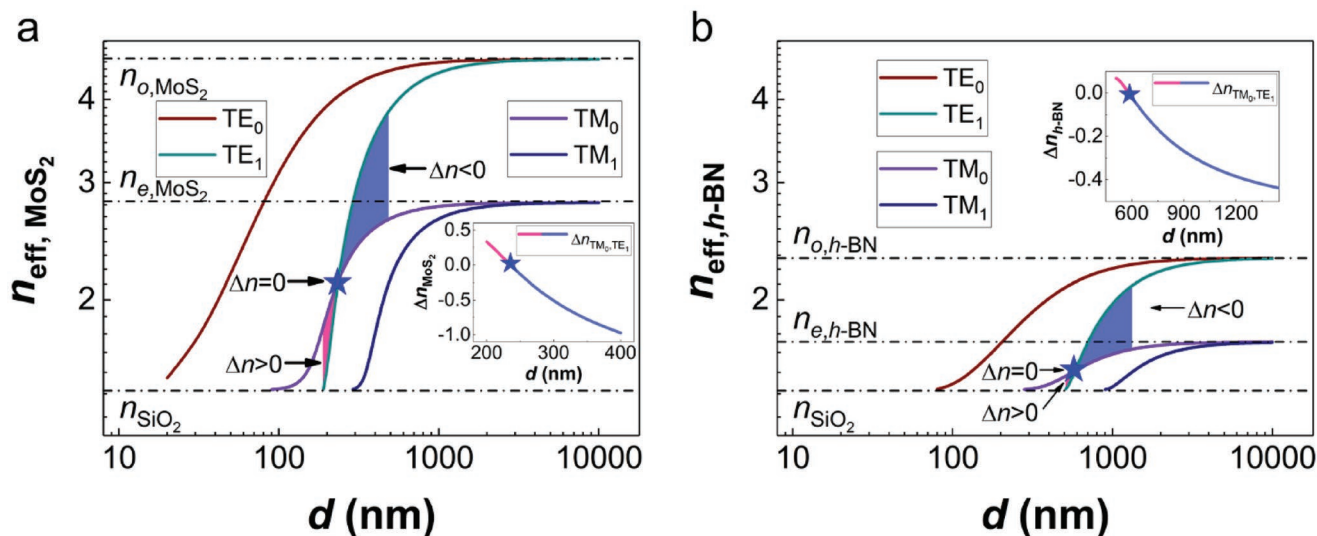


Figure 2. Modal birefringences between orthogonally polarized guided modes in vdW waveguides. a,b) Thickness dispersions of ordinary and extraordinary modes in the air–MoS₂–SiO₂ and air–h-BN–SiO₂ waveguides, respectively. The blue stars indicate the phase matching points of the TM₀ and TE₁ modes in both MoS₂ and h-BN waveguides. On the left side of these critical points, the modal birefringence between TM₀ and TE₁, defined as $\Delta n = n_{\text{eff, TM}_0} - n_{\text{eff, TE}_1}$ is positive, while on the right side Δn is negative. The insets in (a) and (b) show that the modal birefringence in vdW waveguides can be tuned in both sign and magnitude continuously by changing thickness of the guiding layer. The larger the out-of-plane anisotropy the broader the tuning range of the modal birefringence. Note that in both (a) and (b) double logarithmic scales are used.

waveguide, obtained by solving Equations (2) and (3) numerically. There are two intriguing features demonstrated in Figure 2a: the grouping yet noncrossing of guided modes with the same polarization state, and the crossing of guided modes with different polarization states. Specifically, in the limit of d approaching the cutoff thickness of each guided mode, n_{eff} of the relevant mode approaches the substrate refractive index; as d approaches infinity, n_{eff} for the TM (TE) polarized extraordinary (ordinary) modes approaches asymptotically to the value of n_e (n_o). Since $n_e < n_o$ for MoS₂, the l th order TM mode intersects with all the $\geq l + 1$ th TE modes. At the intersection point (indicated by a blue star, $d = 236$ nm), the two orthogonal guided modes share the same effective index of refraction, i.e., being phase matched. At this phase matching point, the modal birefringence between TM₀ and TE₁ defined as $\Delta n = n_{\text{eff, TM}_0} - n_{\text{eff, TE}_1}$ is exactly zero; while it is positive on the left side of this critical point and negative on the right side. Therefore, the modal birefringence between TM₀ and TE₁ is tunable in both sign and magnitude via varying the thickness of the MoS₂ microcrystal. The guided modes in h-BN exhibit similar dispersion behaviors to those in MoS₂, as shown in Figure 2b. However, the tuning range of the resultant modal birefringence is much narrower than that of MoS₂. This is because the maximum tuning range of the modal birefringence is fundamentally limited by the optical anisotropy of the waveguide material: the larger the out-of-plane anisotropy the broader the tuning range of the modal birefringence (this claim can be further confirmed by considering the extreme situation of isotropic guiding layer, i.e., zero material birefringence, see Section S3 in the Supporting Information for details). Since the optical birefringence of h-BN is significantly less than that of MoS₂ at the wavelength of 1530 nm,^[30] the tunability of the modal birefringence in h-BN falls in between the cases of a pure isotropic material and MoS₂. This is another reason why h-BN is inferior to MoS₂ for our proposed applications.

To verify the sign and magnitude bi-tunability of modal birefringence between TM₀ and TE₁ modes in the air–MoS₂–SiO₂ waveguide experimentally, we conducted a series of NIR near-field imaging of MoS₂ microcrystals with thicknesses ranging from 205 to 360 nm in order to encompass the critical thickness $d = 236$ nm. In Figure 3a, we show the fringe profiles of the guided modes in waveguides with different MoS₂ thicknesses (see Section S4 in the Supporting Information for the corresponding near-field images). The indeterminate fringe spacings and the evident beat notes in the near-field profiles strongly indicate the presence of multimode superposition, which can be revealed by Fourier analysis of the data in momentum space.^[30,38] Figure 3b shows the momentum-space spectra of the fringe profiles in Figure 3a. The geometrical factor in the wavevectors has been corrected by shifting all the spectra to the left by a value of $\cos\alpha\sin\beta$. As assigned in Figure 3b, each peak corresponds to a single guided mode or doubly degenerate modes, except for the leftmost ones, which are assigned to the air mode that originates from the residual far-field interferences.^[30,38] All the guided modes shift toward the high spatial frequency direction with the increase of the guiding layer thickness.

The modal birefringence Δn defined above can be experimentally obtained by taking the difference between the peak positions of TM₀ and TE₁. As shown in Figure 4a, Δn is initially positive and decreases with the increasing MoS₂ thickness in the range from 205 to 360 nm ($\Delta n_{205\text{nm}} = +0.30$, $\Delta n_{360\text{nm}} = -0.82$), with the zero-crossing point at a thickness of about 236 nm. At this critical thickness, as the corresponding peaks coincide and merge into a single one in the momentum space (Figure 3b), the TM₀ mode and the TE₁ mode are perfectly phase matched.

The sign and magnitude bi-tunability of the modal birefringence between orthogonally polarized low-loss guided modes is of special interest in the polarization management in integrated

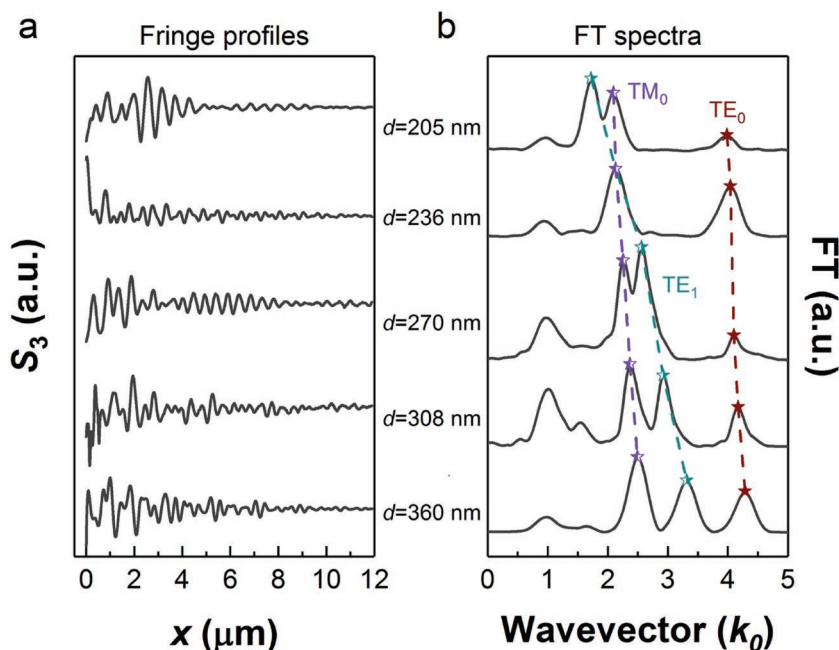


Figure 3. Experimental verification of the sign and magnitude bi-tunability of modal birefringence in the air–MoS₂–SiO₂ three-layer waveguide. a) Fringe profiles of the guided modes corresponding to different MoS₂ thicknesses. b) Momentum-space spectra of the imaged guided modes, obtained by imposing Fourier transform on the near-field fringe profiles in (a). The dash lines correspond to the first three dispersion curves in Figure 2a.

photonic devices. In the case of $\Delta n = 0$, phase matching between the TE polarized ordinary and the TM polarized extraordinary modes (middle panel of Figure 4b) allows a new phase-matching scheme in nonlinear optics.^[42–44] In the case of $\Delta n \neq 0$,

the phase difference between the orthogonally polarized guided modes accumulated in a transmission distance L is $\phi = k_0 \Delta n L$. By choosing suitable transmission distances, on-chip optical phase retardation elements such as quarter- and half-wave plates can be realized. For example, as shown in the upper/lower panel of Figure 4b, the polarization direction of the total electric field of TM₀ and TE₁ modes E would rotate 90 degrees anticlockwise/clockwise after a very short propagation distance about 2.6 μm (zero-order half-wave plates) in the 205/270 nm thick MoS₂ waveguide. This small working-distance is extremely valuable for nano-integrated polarization management applications. For these prospects to come true, interferences from the TE₀ mode and other unwanted modes had better to be eliminated. An ultimate solution is to utilize the degenerate fundamental modes in positive crystals (see Figure S2a in the Supporting Information for details); however, unfortunately, there is no naturally occurred positive vdW crystals known so far. As an alternative approach, we can excite the needed modes selectively using prism coupling or grating coupling methods^[45,46]; in these situations, the TE₀ and other interference modes are no longer a problem.

In summary, the symmetry breaking in layered vdW crystals renders them intrinsically anisotropic in optical responses. Although hyperbolic anisotropy has been under intense studies

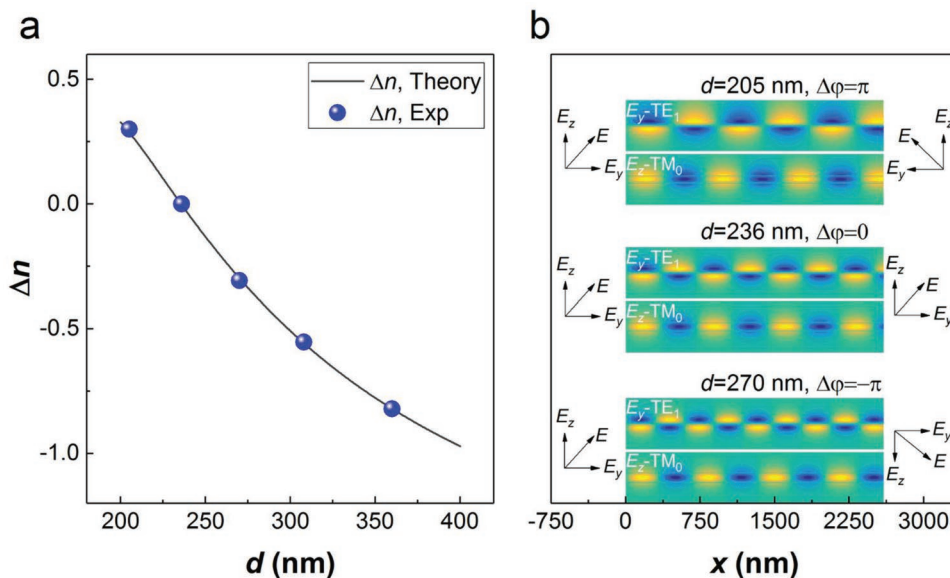


Figure 4. a) Experimentally obtained modal birefringence Δn between the TM₀ and TE₁ guided modes; it can be tuned continuously from positive to negative by varying the guiding layer thickness. The theoretical curve is a duplicate of the inset in Figure 2a. b) Numerical simulations of the real-space electric field distributions associated with TM₀ and TE₁ modes in waveguides with different MoS₂ thicknesses. As a result of the modal birefringence shown in (a), the polarization direction of the total field E tends to change as the modes propagate along the waveguide: only in the case of perfect phase matching (the middle panel) the polarization direction of E can maintain; in the cases of both positive and negative modal birefringences (the upper and lower panels), the polarization direction of E always rotates, anticlockwise and clockwise, respectively.

in recent years, we demonstrate here that the elliptic anisotropy in TMDs is also highly valuable. By using MoS₂ as an example, we show the low-loss transmission of the guided modes as well as the sign- and magnitude-tunable modal birefringence. Our work represents a unique new opportunity to control the polarization behavior of photons in integrated optical circuits at the microscale, with only the thickness of the vdW materials as tuning parameter. Future research can include electrical tuning of the optical birefringence of vdW crystals (e.g., via Kerr effect), seeking for positive vdW crystals ($n_e > n_o$), and geometric designing of channel vdW waveguides, with the goal of achieving tunable modal birefringence between the fundamental (TE₀ and TM₀) guided modes.

Experimental Section

Sample Preparation: Silicon wafers with a 300 nm thick SiO₂ top layer were used as substrates for all samples. The h-BN and MoS₂ microcrystals of various thicknesses were exfoliated from bulk crystals.

Near-Field Optical Measurement: The nanoimaging experiments described in the main text were performed using a commercial s-SNOM (www.neaspec.com). The s-SNOM is based on a tapping-mode AFM illuminated by monochromatic lasers of the wavelength 1530 nm. The near-field images were registered by pseudo-heterodyne interferometric detection module with tip-tapping frequency around 270 kHz, the tip-tapping amplitude is 50 nm for all experiments. By demodulating the optical signal at the third-order harmonic of the tip-tapping frequency, the noise from the background and stray light can be greatly suppressed.

Supporting Information

Supporting Information is available from the Wiley Online Library or from the author.

Acknowledgements

This work was supported by the National Basic Key Research Program of China (No. 2015CB932400 and 2016YFA0202000), the National Natural Science Foundation of China (Nos. 11704085, 51372045, 11504063, and 11674073), and the Key Program of the Bureau of Frontier Sciences and Education Chinese Academy of Sciences (No. QYZDB-SSWSLH021).

Conflict of Interest

The authors declare no conflict of interest.

Keywords

near-field imaging, optical anisotropy, phase retardation, planar waveguides, polarization management

Received: December 3, 2018

Revised: April 18, 2019

Published online:

- [1] J. D. Sarmiento-Merenguel, R. Halir, X. Le Roux, C. Alonso-Ramos, L. Vivien, P. Cheben, E. Durán-Valdeiglesias, I. Molina-Fernández, D. Marris-Morini, D. X. Xu, J. H. Schmid, S. Janz, A. Ortega-Moñux, *Optica* **2015**, *2*, 1019.
- [2] S. Liao, W. Cai, J. Handsteiner, B. Liu, J. Yin, L. Zhang, D. Rauch, M. Fink, J. Ren, W. Liu, Y. Li, Q. Shen, Y. Cao, F. Li, J. Wang, Y. Huang, L. Deng, T. Xi, L. Ma, T. Hu, L. Li, N. Liu, F. Koidl, P. Wang, Y. Chen, X. Wang, M. Steindorfer, G. Kirchner, C. Lu, R. Shu, R. Ursin, T. Scheidl, C. Peng, J. Wang, A. Zeilinger, J. Pan, *Phys. Rev. Lett.* **2018**, *120*, 30501.
- [3] M. Born, E. Wolf, *Principles of Optics*, Cambridge University Press, Cambridge, UK **1999**.
- [4] A. Yariv, P. Yeh, *Optical Waves in Crystals: Propagation and Control of Laser Radiation*, Wiley, Hoboken, NJ, USA **2003**.
- [5] N. Wang, X. Liu, Q. Xiong, J. Xie, S. Chen, L. Liu, *Opt. Lett.* **2017**, *42*, 2996.
- [6] C. Wang, M. Zhang, X. Chen, M. Bertrand, A. Shams-Ansari, S. Chandrasekhar, P. Winzer, M. Lončar, *Nature* **2018**, *562*, 101.
- [7] Y. Zhang, Y. He, Q. Zhu, X. Jiang, X. Guo, C. Qiu, Y. Su, *Front. Optoelectron.* **2018**, *11*, 77.
- [8] R. J. Black, L. Gagnon, *Optical Waveguide Modes: Polarization, Coupling and Symmetry*, McGraw-Hill, New York **2010**.
- [9] J. Schollhammer, M. A. Baghban, K. Gallo, *Opt. Lett.* **2017**, *42*, 3578.
- [10] D. Dai, L. Liu, S. Gao, D. Xu, S. He, *Laser Photonics Rev.* **2013**, *7*, 303.
- [11] K. S. Novoselov, A. Mishchenko, A. Carvalho, A. H. Castro Neto, *Science* **2016**, *353*, aac9439.
- [12] W. Y. Liang, *J. Phys. C: Solid State Phys.* **1973**, *6*, 551.
- [13] S. Dai, Z. Fei, Q. Ma, A. S. Rodin, M. Wagner, A. S. McLeod, M. K. Liu, W. Gannett, W. Regan, K. Watanabe, T. Taniguchi, M. Thiemens, G. Dominguez, A. H. C. Neto, A. Zettl, F. Keilmann, P. Jarillo-Herrero, M. M. Fogler, D. N. Basov, *Science* **2014**, *343*, 1125.
- [14] J. D. Caldwell, A. V. Kretinin, Y. Chen, V. Giannini, M. M. Fogler, Y. Francescato, C. T. Ellis, J. G. Tischler, C. R. Woods, A. J. Giles, M. Hong, K. Watanabe, T. Taniguchi, S. A. Maier, K. S. Novoselov, *Nat. Commun.* **2014**, *5*, 5221.
- [15] Z. Zheng, J. Chen, Y. Wang, X. Wang, X. Chen, P. Liu, J. Xu, W. Xie, H. Chen, S. Deng, N. Xu, *Adv. Mater.* **2018**, *30*, 1705318.
- [16] W. Ma, P. Alonso-González, S. Li, A. Y. Nikitin, J. Yuan, J. Martín-Sánchez, J. Taboada-Gutiérrez, I. Amenabar, P. Li, S. Vélez, C. Tollan, Z. Dai, Y. Zhang, S. Sriram, K. Kalantar-Zadeh, S. Lee, R. Hillenbrand, Q. Bao, *Nature* **2018**, *562*, 557.
- [17] K. Khaliji, A. Fallahi, L. Martin-Moreno, T. Low, *Phys. Rev. B* **2017**, *95*, 201401.
- [18] J. S. Toll, *Phys. Rev.* **1956**, *104*, 1760.
- [19] K. R. Waters, J. Mobley, J. G. Miller, *IEEE Trans. Ultrasonics, Ferroelectr. Freq. Control* **2005**, *52*, 822.
- [20] D. N. Basov, M. M. Fogler, F. J. García De Abajo, *Science* **2016**, *354*, aag1992.
- [21] T. Low, A. Chaves, J. D. Caldwell, A. Kumar, N. X. Fang, P. Avouris, T. F. Heinz, F. Guinea, L. Martin-Moreno, F. Koppens, *Nat. Mater.* **2017**, *16*, 182.
- [22] C. H. Perry, G. Rupprecht, R. Geick, *Phys. Rev.* **1966**, *146*, 543.
- [23] M. N. Gjerding, R. Petersen, T. G. Pedersen, N. A. Mortensen, K. S. Thygesen, *Nat. Commun.* **2017**, *8*, 320.
- [24] J. Son, J. Kwon, S. Kim, Y. Lv, J. Yu, J. Lee, H. Ryu, K. Watanabe, T. Taniguchi, R. Garrido-Menacho, N. Mason, E. Ertekin, P. Y. Huang, G. Lee, A. M. Van Der Zande, *Nat. Commun.* **2018**, *9*, 3988.
- [25] J. Shim, S. Bae, W. Kong, D. Lee, K. Qiao, D. Nezich, Y. J. Park, R. Zhao, S. Sundaram, X. Li, H. Yeon, C. Choi, H. Kum, R. Yue, G. Zhou, Y. Ou, K. Lee, J. Moodera, X. Zhao, J. Ahn, C. Hinkle, A. Ougazzaden, J. Kim, *Science* **2018**, *362*, 665.
- [26] Q. H. Wang, K. Kalantar-Zadeh, A. Kis, J. N. Coleman, M. S. Strano, *Nat. Nanotechnol.* **2012**, *7*, 699.

- [27] R. Ganatra, Q. Zhang, *ACS Nano* **2014**, *8*, 4074.
- [28] S. Wang, H. Yu, H. Zhang, A. Wang, M. Zhao, Y. Chen, L. Mei, J. Wang, *Adv. Mater.* **2014**, *26*, 3538.
- [29] F. Yu, Q. Liu, X. Gan, M. Hu, T. Zhang, C. Li, F. Kang, M. Terrones, R. Lv, *Adv. Mater.* **2017**, *29*, 1603266.
- [30] D. Hu, X. Yang, C. Li, R. Liu, Z. Yao, H. Hu, S. N. G. Corder, J. Chen, Z. Sun, M. Liu, Q. Dai, *Nat. Commun.* **2017**, *8*, 1471.
- [31] G. Ghosh, *Opt. Commun.* **1999**, *163*, 95.
- [32] S. Niu, G. Joe, H. Zhao, Y. Zhou, T. Orvis, H. Huyen, J. Salman, K. Mahalingam, B. Urwin, J. Wu, Y. Liu, T. E. Tiwald, S. B. Cronin, B. M. Howe, M. Mecklenburg, R. Haiges, D. J. Singh, H. Wang, M. A. Kats, J. Ravichandran, *Nat. Photonics* **2018**, *12*, 392.
- [33] F. Keilmann, R. Hillenbrand, *Philos. Trans. R. Soc. A* **2004**, *362*, 787.
- [34] N. Ocelic, A. Huber, R. Hillenbrand, *Appl. Phys. Lett.* **2006**, *89*, 101124.
- [35] Z. Fei, A. S. Rodin, G. O. Andreev, W. Bao, A. S. McLeod, M. Wagner, L. M. Zhang, Z. Zhao, M. Thiemens, G. Dominguez, M. M. Fogler, A. H. C. Neto, C. N. Lau, F. Keilmann, D. N. Basov, *Nature* **2012**, *487*, 82.
- [36] J. Chen, M. Badioli, P. Alonso-Gonzalez, S. Thongrattanasiri, F. Huth, J. Osmond, M. Spasenovic, A. Centeno, A. Pesquera, P. Godignon, A. Z. Elorza, N. Camara, D. A. F. Garcia, R. Hillenbrand, F. H. Koppens, *Nature* **2012**, *487*, 77.
- [37] G. X. Ni, A. S. McLeod, Z. Sun, L. Wang, L. Xiong, K. W. Post, S. S. Sunku, B. Y. Jiang, J. Hone, C. R. Dean, M. M. Fogler, D. N. Basov, *Nature* **2018**, *557*, 530.
- [38] Z. Fei, M. E. Scott, D. J. Gosztola, J. J. Foley, J. Yan, D. G. Mandrus, H. Wen, P. Zhou, D. W. Zhang, Y. Sun, J. R. Guest, S. K. Gray, W. Bao, G. P. Wiederrecht, X. Xu, *Phys. Rev. B* **2016**, *94*, 81402.
- [39] J. Hu, C. R. Menyuk, *Adv. Opt. Photonics* **2009**, *1*, 58.
- [40] D. M. Shyroki, A. V. Lavrinenko, *J. Opt. A: Pure Appl. Opt.* **2003**, *5*, 192.
- [41] K. Kawano, T. Kitoh, *Introduction to Optical Waveguide Analysis*, John Wiley & Sons, New York **2001**.
- [42] R. Normandin, G. I. Stegeman, *Opt. Lett.* **1979**, *4*, 58.
- [43] T. Suhara, M. Fujimura, *Waveguide Nonlinear-Optic Devices*, Springer, New York **2003**.
- [44] A. Autere, H. Jussila, Y. Dai, Y. Wang, H. Lipsanen, Z. Sun, *Adv. Mater.* **2018**, *30*, 1705963.
- [45] B. M. Trabold, D. Novoa, A. Abdolvand, P. S. J. Russell, *Opt. Lett.* **2014**, *39*, 3736.
- [46] W. S. Mohammed, A. Mehta, M. Pitchumani, E. G. Johnson, *IEEE Photonics Technol. Lett.* **2005**, *17*, 1441.